Optica Applicata, Vol. LIV, No. 3, 2024
DOI: 10.37190/oa240301

Propagation of laser modes by testing the angular spectrum technique and the analysis of Gaussian beam profiles by using the multiple knife-edge method

ALEXANDER TALATINIAN

Department of Optics and Photonics, Faculty of Fundamental Problems of Technology,
Wroclaw University of Science and Technology,
Wybrzeze Wyspianskiego 27, 50-370 Wroclaw, Poland;
e-mail: alexander.talatinian@pwr.edu.pl

This research focuses on the analysis of laser beam shape propagation properties and the generalized beam shaping of the fundamental Gaussian mode, Hermite–Gaussian modes and Laguerre –Gaussian modes, which were studied analytically and numerically using the angular spectrum technique and the 2D fast Fourier transformation procedures. The fundamental Gaussian mode is applied here as the reference for checking the accuracy of beam profile analysis based on multiple scanning knife-edge method. A set of spatial profile curves is generated, each of which represents the intensity profile of the fundamental Gaussian mode for different directions of propagation. The He-Ne laser and the diode laser are used as the probe lasers. The experimental results show that the He-Ne laser emits a pure fundamental Gaussian mode, whereas the diode laser emits an elliptical beam shape. Some numerical simulation examples of the generated beams are also given to illustrate the propagation properties of the fundamental Gaussian mode, Hermite–Gaussian modes, and Laguerre–Gaussian modes.

Keywords: laser beam analysis, multiple knife-edge, propagation of higher modes, angular spectrum algorithm.

1. Introduction

In laser applications, it is important to be able to modify the properties of beams, and to collimate, expand, shape, focus, *etc*. by using lenses or other optical elements. It is necessary to know the laser beam's parameters, such as beam waist, far field divergence, wavefront curvature, beam width, and the parameter M^2 – a multimode beam quality factor that can describe both the quality of a laser beam as well as its propagation. In the general case, a laser application requires a laser beam with low divergence that is emitted in the so-called fundamental Gaussian mode (FGM), and a laser beam that emits a pure Gaussian beam (GB) profile [1-4]. This FGM has the lowest possible

value of $M^2 = 1$ and can usually be derived as the mode with the minimum transverse spatial extension at the minimum beam divergence. However, this feature is not always guaranteed, particularly for high power lasers, since the emission occurs in various modes. In this case, the laser beam emerging from the optical resonator can be completely obtained as a superposition of Hermite–Gaussian modes (HGMs) with regard to Cartesian coordinates, or by Laguerre–Gaussian modes (LGMs) with regard to cylindrical coordinates. They are eigenmodes of the paraxial wave equation and both sets of transverse modes are acceptable forms of the transverse distribution of the complex amplitude field within stable laser resonators [5-7]. It follows from the above that the intensity distribution is different from the FGMs, and any deviation from the ideal diffraction-limited GB profile can be attributed to the contribution of higher order modes with more complicated intensity distributions, leading to $M^2 > 1$. Thus, a real beam is always larger than the suggested FGM and the desired performance requirements in applications are not fulfilled [8]. There are some methods to analyze a laser beam, its quality profile, and intensity, such as Camera-based systems CCD, scanning aperture, burn spot, photographic technique, the slit scan method, the pinhole method, the variable -aperture method, the knife-edge scan method and the second-moment method [9-17]. All these methods are reliable for pure GBs, but suffer from various errors when applied to non-Gaussian beam shapes, where the beam is astigmatic and has an elliptical cross -section. Among the methods, the scanning knife-edge one belongs to those that are most widely used (for a long time now) and it is regarded as a standard technique for GB characterization [18-21]. Moreover, some other methods have also been developed, like photothermal deflection [22] and the thermographic technique [23]. Owing to its simplicity, however, the knife-edge method (KEM) has gained popularity in measuring the FGM and beams with arbitrary intensity distributions [24,25]. On the other hand, tomographic techniques based on KEM have been applied to determine the intensity distribution along the propagation of a laser beam [26-29]. The background of the conventional KEM is the scalar diffraction theory, and therefore in the standard knife-edge test, the beam is focused by the test element and the shadow patterns are obtained when the knife-edges moves along the laser beam direction, blocking out about half of the beam, while the power of the transmitted beam is monitored by a detector [30]. The observed shadow patterns are different depending on the position of the inserted knife -edge in the beam and the test surface. Usually, the knife-edge is placed at three positions – before the focal plane, then at the focal plane, and the third one behind it – where shadow patterns are observed [31]. In this work, the spatial beam intensity profile is measured by a beam analyzer head "BeamMaster" PC. It also measures the widths, peak location, centroid lactation, position, total optical power, and basic beam shape of CW lasers. Multiple knife-edges are used to scan across the beam path in different axes as the drum rotates. The intensity distribution of the laser beam is captured using the mathematical process known as "Reconstructive Tomography", yielding a displayed resolution of 32 × 32 regardless of the beam size. The same procedure is used by X-ray systems to create X-rays images. As probe lasers, the He-Ne laser emitting a symmetrical shape beam or pure GB, or the diode laser emitting an elliptical shape

beam are used. The diode laser often emits astigmatic beams with large divergence, which causes their transformation to be more complex. The angular plane wave spectrum method has been applied to calculate the propagation of the FGM, HGM and LGM [32-35], as well as to model the propagation of the optical vortex beam [36-40]. This work is an extension of our previous work [34] and is focused on implementing the angular spectrum method (ASM) with the application of the 2D fast Fourier transform (FFT). The whole numerical procedure will be called here AS FFT method, which can be used to model any physically realizable beam, such as GBs, HGBs, and LGBs, whether the beam has an analytical representation or not.

2. Angular spectrum algorithm

The AS a technique, in combination with the Fourier decomposition of the wave field, makes use of elementary solutions in the form of planar waves and evanescend waves [41]. As with the Rayleigh–Sommerfeld formulation, the AS optical propagation technique models a wave that propogates from an initial plane at z_0 to a parallel observation plane at z, where z is the propagation direction. As with all wave fields, it is calculated using the AS FFT algorithm, which uses the 2D FFT procedure. This is done as follows. Firstly, we apply a 2D FT at the stage of decomposition of the initial wave field to Fourier amplitudes; secondly, we multiply those amplitudes with a propagation factor over the distance z; and thirdly, we apply an inverse Fourier transformation (IFT), which yields the wave field distribution in the observation plane $z > 0$, which can be written in the form

$$E_z(x, y; z) = \int_{-\infty}^{+\infty}\int_{-\infty}^{+\infty} \left\{ \begin{aligned} &\tilde{E}_0(v_x, v_y; z_0) \exp\left[\mathrm{i}2\pi z \sqrt{\frac{1}{\lambda^2} - v_x^2 - v_y^2} \right] \\ &\qquad \times \exp\left[2\pi \mathrm{i}(v_x x + v_y y) \right] \end{aligned} \right\} \mathrm{d}v_x \, \mathrm{d}v_y \qquad (1)$$

where $\tilde{E}_0(v_x, v_y; z_0)$ is the complex amplitude distribution in the initial plane, defined by $E_0(v_x, v_y; z = 0) = \mathrm{F}_{2\mathrm{D}}\{E_0(x, y; z = 0)\}$, λ is the wavelength of light, z is the propagation distance, v_x, v_y are the spatial frequencies in Fourier domain along the x- and y-axes. The above formula is the near-field and the far-field expression for the propagation of the wave field.

3. Hermith and Laguerre–Gaussian modes families

Many lasers in the laboratory emit a pure FGM and a beam quality factor equal to 1. However, in some lasers, such as a diode laser, optical resonators emit higher order modes, which causes the multimode beam quality factor parameter to be greater than that of a pure FGM of the value $M^2 > 1$. The above formula is appropriate for laser beams which have an elliptical beam shape around the propagation axis z. Such beams

are called astigmatic because the position of the beam waist along the axis of propagation is normally different within the two principal planes *XZ*, *YZ* and the set of two-beam parameters W_{0x} and W_{0y}. In this case, the complex amplitude profile distribution of HG_{mn}, determined by the two beam waist spot size $W_{0\,x,y}$, light wavelength λ, and beam order modes *m* and *n*, is given by

$$\psi_{mn}^{\mathrm{HG}}(x,y,z) = E_0 \frac{\sqrt{W_{0x}W_{0y}}}{W_x(z)W_y(z)} H_m\left(\frac{\sqrt{2}\,x}{W_x(z)}\right) H_{mn}\left(\frac{\sqrt{2}\,y}{W_y(z)}\right) \exp\left[-\frac{x^2}{W_x^2(z)} - \frac{y^2}{W_y^2(z)}\right]$$

$$\times \exp\left\{\mathrm{i}\left[kz + \frac{\pi x^2}{\lambda R_x(z)} + \frac{\pi y^2}{\lambda R_y(z)} - (m+n+1)\varphi_{\mathrm{G}}(z)\right]\right\} \tag{2}$$

Here, W_{0x} and W_{0y} are the waist spot sizes in the *x* and *y* directions, and $W_x(z)$ and $W_y(z)$ are the beam widths in the *x* and *y* directions, respectively. For rectangular symmetry, we can separate the two transversal components *x* and *y* and obtain a solution for each one, that is, the product of a Gaussian function with a Hermite polynomials H_m, H_n which are called HG_{mn} modes [42]:

$$\psi_{nm}^{\mathrm{HG}}(x,y,z) = E_0 \frac{W_0}{W(z)} H_n\left(\frac{\sqrt{2}\,x}{W(z)}\right) H_m\left(\frac{\sqrt{2}\,y}{W(z)}\right) \exp\left[-\frac{x^2+y^2}{W^2(z)}\right]$$

$$\times \exp\left\{-\mathrm{i}\left[kz + \frac{\pi(x^2+y^2)}{\lambda R(z)} - (m+n+1)\varphi_{\mathrm{G}}(z)\right]\right\} \tag{3}$$

and the intensity distribution of the HG_{mn} mode is given in the form

$$I_{nm}^{\mathrm{HG}}(x,y,z) = E_0^2 \frac{W_0^2}{W^2(z)} H_n^2\left(\frac{\sqrt{2}\,x}{W(z)}\right) H_m^2\left(\frac{\sqrt{2}\,y}{W(z)}\right) \exp\left[-2\frac{x^2+y^2}{W^2(z)}\right] \tag{4}$$

In the above expressions, the HGBs' functions alternate between even and odd symmetry when altering the *m* and *n* modes. The lowest order of HGBs is obtained from Eq. (3) with setting $n = m = 0$. Since the Hermite polynomial of zero order is a constant, Eq. (3) reduces to the Gaussian beam, which is called FGM form:

$$E_{\mathrm{G}}(x,y,z) = E_0 \frac{W_0}{W(z)} \exp\left[-\frac{x^2+y^2}{W^2(z)}\right] \exp\left[-\mathrm{i}\frac{\pi(x^2+y^2)}{\lambda R(z)}\right] \exp\left\{-\mathrm{i}\left[kz - \varphi_{\mathrm{G}}(z)\right]\right\} \tag{5}$$

where W_0 is the $1/e$ width of the GB in the waist plane $z = 0$, E_0 is the peak electric field amplitude, $W(z) = W_0[1 + (\lambda z/\pi W_0^2)^2]^{1/2}$ is the beam width that varies with

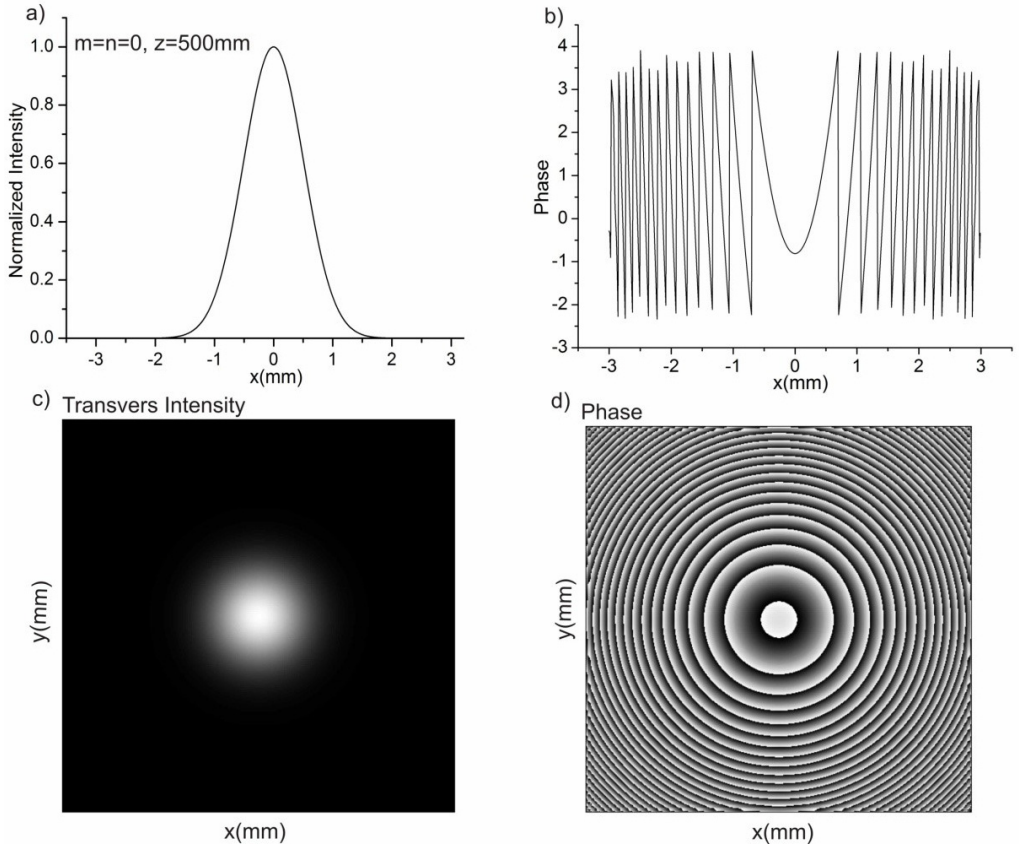

Fig. 1. AS FFT calculations of the FGM showing normalized intensity distribution (a), phase distribution (b), transverse cross-section intensity distribution (c), and phase distribution in a plane cross-section (d). Calculations are performed for $m = n = 0$, $W_0 = 0.1$ mm, $\lambda = 632.8$ nm, $D = 6$ mm, and $z = 500$ mm.

the distance z, $R(z) = z[1 + (\pi W_0^2/\lambda z)^2]^{1/2}$ is the radius of the wavefront curvature as a function of the longitudinal position z, $\varphi_G(z) = -\arctan(\lambda z/\pi W_0^2)$ is the Gouy phase shift, $z_R = \pi W_0^2/\lambda$ is the Rayleigh range used to measure the distance over which the beam remains well collimated, and $\theta_0 = \lambda/\pi W_0$ is the divergence angle for an ideal, diffraction limited beam. The examples of the normalized intensity and phase distributions of the FGM are shown in Fig. 1(a,b), and the transverse intensity and phase distributions in the plane X, Y cross-section of the AS FFT algorithm at the observation plane are shown in Fig. 1(c,d).

The results of the numerical calculations of the FGM along the propagation distance z, using the AS FFT method and the 2D FFT, are shown in Fig. 2. The Gouy phase shift $\varphi_G(z)$ and modulated phase $\Phi(z) = -kz + \varphi_G(z)$ noise are visible around the beam waist in Fig. 2 (e,f). However, this only occurs in the areas of very low beam amplitude, so the error in the complex amplitude field value is relatively small. It is visible that the imaginary part of the complex amplitude field changes its sign near the plane

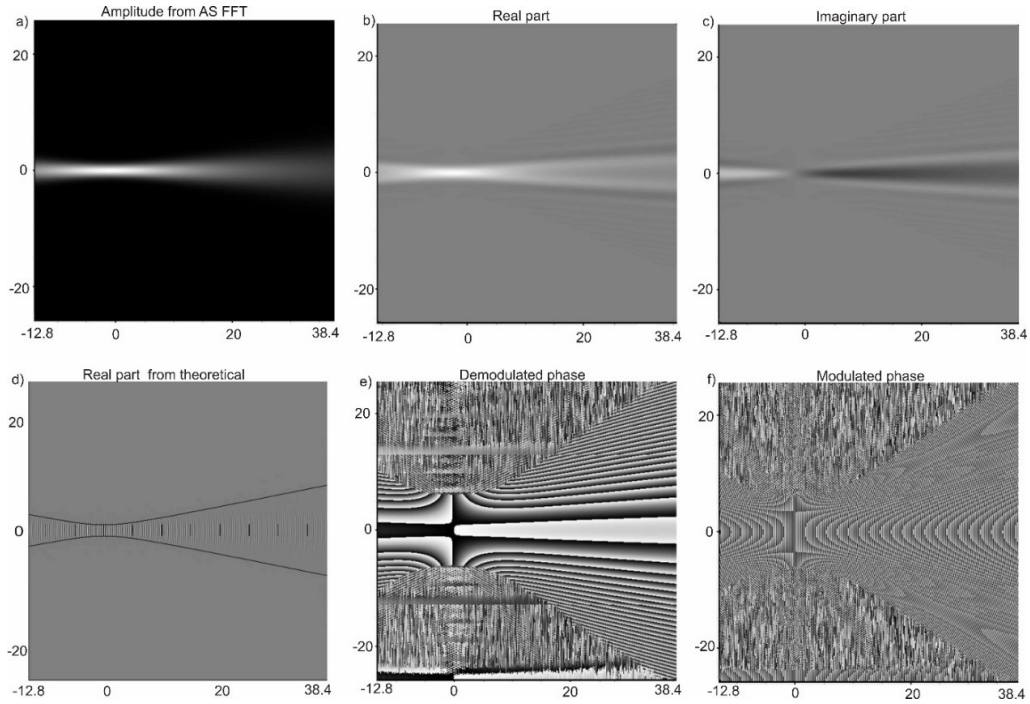

Fig. 2. Gaussian beam optical field magnitude distribution cross-section in the YZ plane of $W_0 = 1$ μm, calculated in the range of –12.8 to 38.4 μm. (b) Real part of the GB optical field distribution in the YZ plane. (c) Imaginary part of the GB optical field distribution in the YZ plane. (d) Superposition of the real part of the optical field with the theoretically calculated beam profile. Vertical lines show the positions of $z = n \times z_R$, where n – integers ($n = 0$ at the waist). (e) GB optical field $E_G(x, y, z)$ demodulated phase distribution in the YZ plane after the removal of the free propagating wave phase $\exp(-ikz)$. (f) GB optical field $E_G(x, y, z)\exp(-ikz)$ phase distribution in the YZ plane. Calculations are performed for $\lambda = 632.8$ nm, $W_0 = 1$ μm, $D = 50$ μm.

$z = 0$, which is the reason why the demodulated Gouy phase shift and modulated phase are visible along the z axis. As can be clearly seen in Fig. 2(f), the wavefront curvatures are very dense, and the phase lines, which should be close to the spherical form (with beam front radius), show complicated shapes with sampling in the image because of the Moiré effect.

An examples of the 2D and 3D normalized transverse intensity distributions of the HG_{mn} modes are presented in Fig. 3. Note that the transverse intensity distribution of the HG_{24} beam consists of m nodes (intensity nulls) and $(m + 1)$ lobes in the x direction, and n nodes and $(n + 1)$ lobes in the y direction, at each of which the phase undergoes a jump of π radians in the direction perpendicular to the node. In addition, as can be seen in Fig. 3, the rectangular shape also becomes more noticeable as the mode number is increased.

The simulation results of the transverse cross-sectional amplitude distribution and its propagation, and the 2D amplitude distribution profiles in the sagittal observation

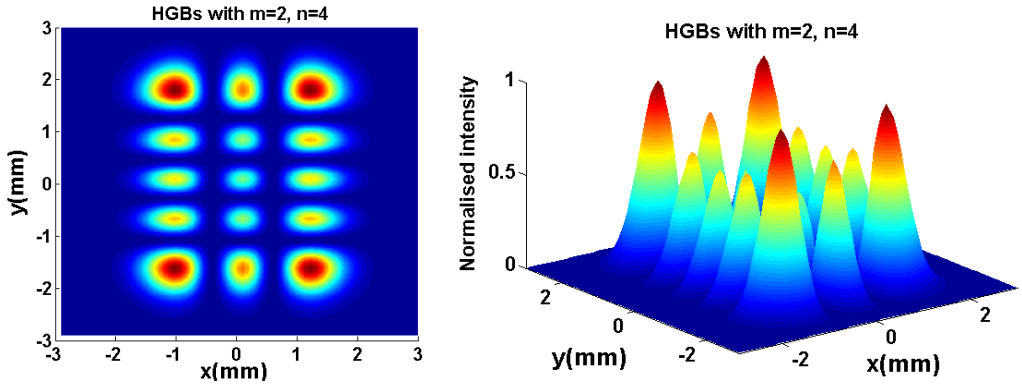

Fig. 3. The normalized transverse intensity distribution of the 2D and 3D HGB at the observation plane $z = 0$. Calculations were performed for the HG_{24}, $W_0 = 1$ mm, $\lambda = 632.8$ mm, and $D = 6$ mm.

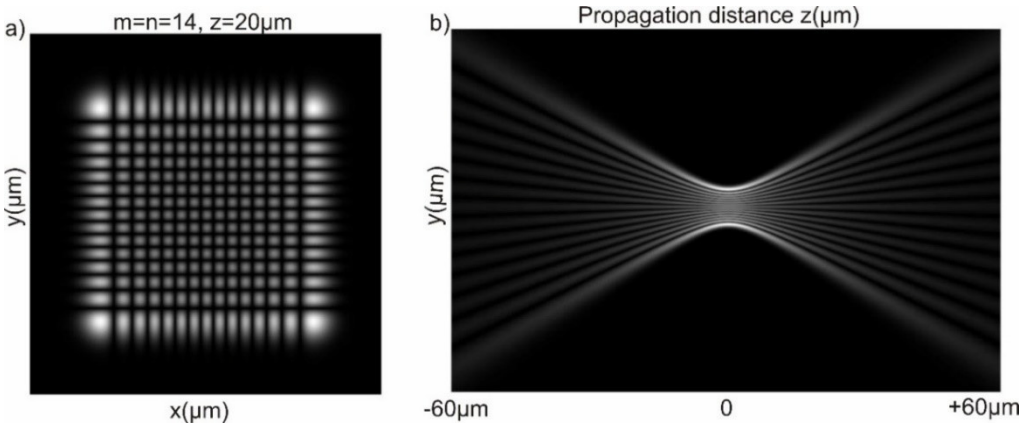

Fig. 4. (a) Transverse cross-section showing the amplitude distribution of the HG_{1414} mode at the $z = 60$ μm observation plane. (b) The 2D propagation amplitude distribution profiles in the YZ observation plane. The numerical simulation uses AS FFT algorithm with $W_0 = 0.8$ μm, and $\lambda = 632.8$ nm.

plane for the HG_{1414} mode propagating along the longitudinal z axis for different values of the propagation distance z and obtained using the AS FFT algorithm are shown in Fig. 4.

According to Eq. (3), the full phase term is given by

$$\Phi_{\mathrm{HG}}(x, y, z) = \exp\left[\mathrm{i}(m + n + 1)\varphi_{\mathrm{G}}(z)\right]\exp\left[-\frac{\mathrm{i}\pi(x^2 + y^2)}{\lambda R(z)}\right]\exp[-ikz] \qquad (6)$$

where $\exp[\mathrm{i}(m + n + 1)\varphi_{\mathrm{G}}(z)]$ is the Gouy phase shift factor of the HG_{mn} mode. Figures 5 and 6 show the transverse intensity and phase distributions of several HG_{mn} modes. The black color corresponds to zero intensity and zero phase, the white color corresponds to maximal intensity, and the gray color corresponds to maximal phase 2π.

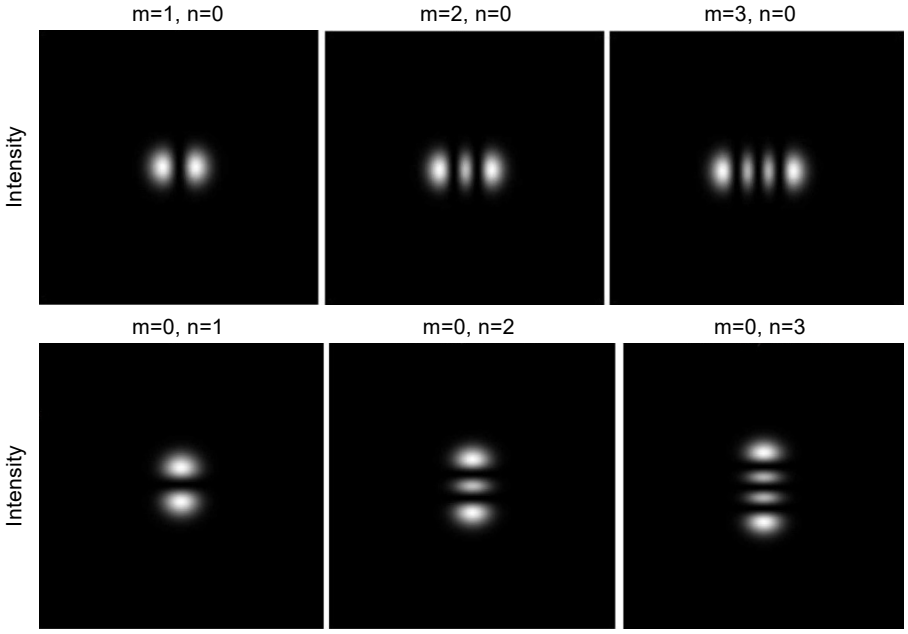

Fig. 5. Transverse cross-section showing the spatial profiles of the intensity distributions of six various HG_{mn} modes. The numerical simulation calculation was performed for $z = 0$, $W_0 = 0.5$ mm, $\lambda = 632.8$ mm, and the diameter of each plot is $D = 6$ mm.

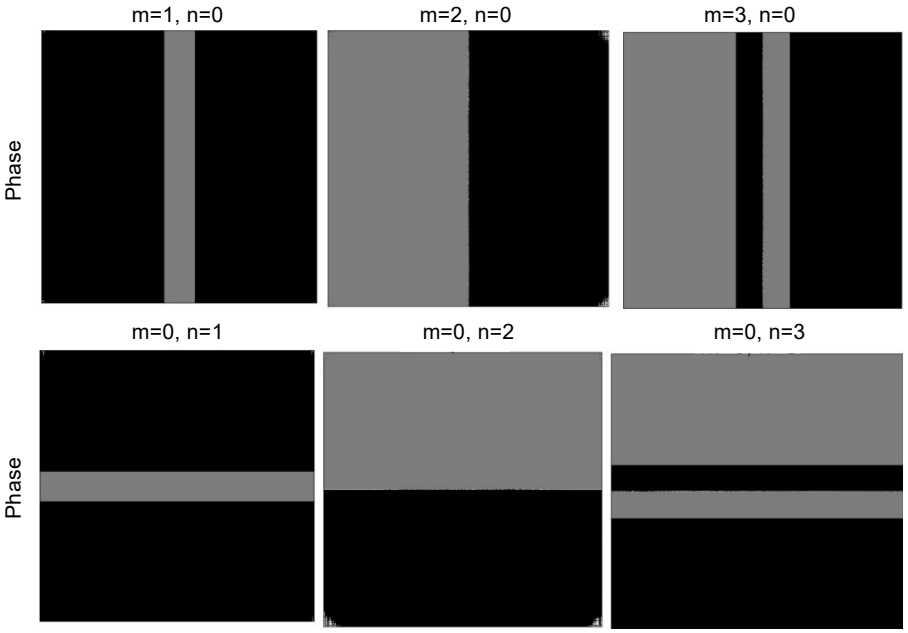

Fig. 6. Phase distribution of the HGBs in a plane cross-section of various HG_{mn} modes, with the same parameters used as in Fig. 5.

These modes are structurally stable, which means that their intensity profiles remain the same on propagation, which contrast with LG_{pl} modes.

The shape of any paraxial beam can also be described as a sum of LG_{pl} modes, which are a complete and orthogonal set of solutions for the paraxial wave equation, and can be represented in cylindrical coordinates (ρ, φ, z) along the propagation axis z. Mathematically, they are described by the expression [43-47]

$$E_{pl}^{\mathrm{LG}}(\rho, \varphi, z) = E_0 \frac{w_0}{w(z)} \left(\frac{\sqrt{2}\,\rho}{w(z)} \right)^{|l|} L_p^l \left[2 \left(\frac{\rho}{W(z)} \right)^2 \right] \exp\left[\mathrm{i}(2p + |l| + 1)\varphi_{\mathrm{G}}(z) \right]$$

$$\times \exp\left[-\left(\frac{\rho}{W(z)} \right)^2 \right] \exp\left[-\frac{\mathrm{i}\pi\rho^2}{\lambda R(z)} \right] \exp(-\mathrm{i}kz) \exp[-\mathrm{i}l\varphi] \tag{7}$$

where L_p^l represents the Laguerre polynomials defined by the radial mode p, a non-negative integer, which determines the number of nodes along the radial direction and the azimuthal mode l. The azimuthal mode l determines the phase distribution around the azimuthal direction and may take any integer value, either positive or negative, and is associated with the vortex term; $\rho = (x^2 + y^2)^{1/2}$ is a cylindrical radius, φ is the azimuthal angle, and the rest of the parameters are the same as in the FGM. The characteristic feature of these modes is the azimuthal transverse phase structure $\exp[-\mathrm{i}l\varphi]$, which gives rise to the helical wavefront and nonzero orbital angular momentum (OAM) of the beam given as $l\hbar$ per photon. In the plane of the beam waist $z = 0$, the real amplitude field of the LGMs simplifies to

$$E_{pl}^{\mathrm{LG}}(\rho, z = 0) = E_0 \left(\frac{\sqrt{2}\,\rho}{w_0} \right)^{|l|} L_p^l \left[2 \left(\frac{\rho}{w_0} \right)^2 \right] \exp\left[-\left(\frac{\rho}{w_0} \right)^2 \right] \tag{8}$$

According to Eq. (7), the distribution of field intensity of the LGBs is given by

$$I_{pl}^{\mathrm{LG}}(\rho, z) = E_0^2 \frac{w_0^2}{w^2(z)} \left(\frac{2\rho^2}{w^2(z)} \right)^{|l|} L_{pl}^2 \left[2 \left(\frac{\rho}{w(z)} \right)^2 \right] \exp\left[-\left(\frac{2\rho}{w(z)} \right)^2 \right] \tag{9}$$

While the full phase term is given by

$$\Phi_{\mathrm{LG}}(\rho, \varphi, z) = \exp\left[\mathrm{i}(2p + |l| + 1)\varphi_{\mathrm{G}}(z) \right] \exp\left[-\frac{\mathrm{i}\pi\rho^2}{\lambda R(z)} \right] \exp(-\mathrm{i}kz) \exp[-\mathrm{i}l\varphi] \tag{10}$$

where $\exp[\mathrm{i}(2p + |l| + 1)\varphi_{\mathrm{G}}(z)]$ represents a Gouy phase shift factor of the LG_{pl} mode, which is associated with the focusing of the beam at the waist plane [48,49]. The magnitude of the Gouy phase change thus depends on the radial and azimuthal modes. Figures 7 and 8 show the transverse intensity distributions and spatial phase profiles of

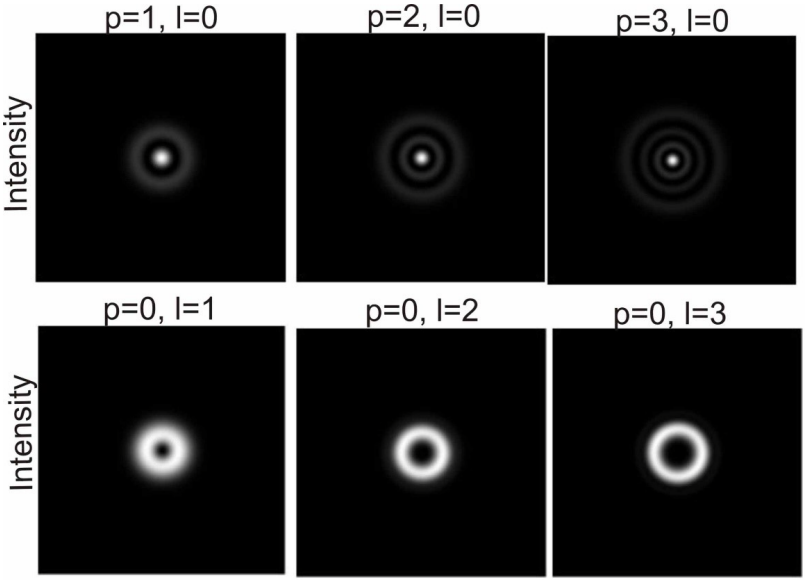

Fig. 7. Transverse cross-section showing the spatial profiles of the intensity distributions of six various LG_{pl} modes at the waist plane $z = 0$ for different azimuthal number modes and radial modes, and with the same parameters as in Fig. 5.

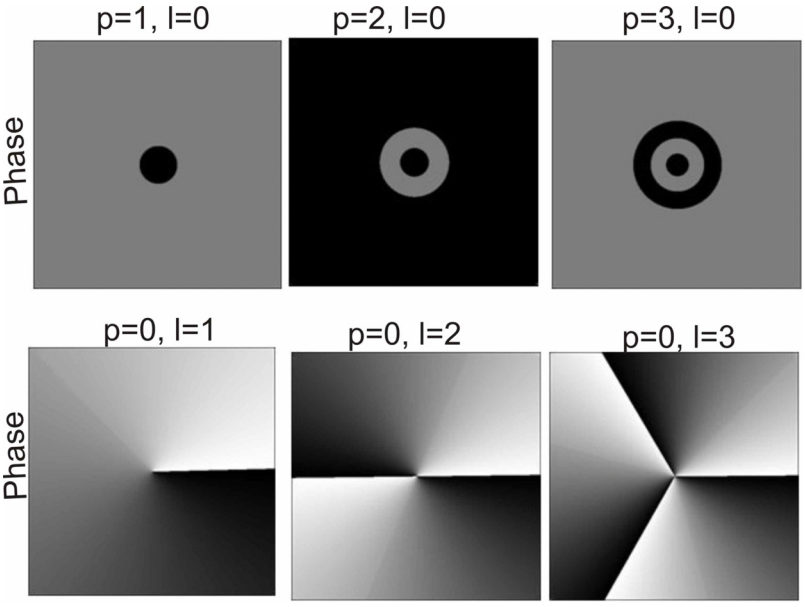

Fig. 8. Phase profiles of the LGBs in a plane cross-section with different azimuthal and radial modes. The total phase change of one rotation is exactly 2π, 4π, and 6π, respectively (second row). In three cases, the only real phase discontinuity of significance is on the beam axis. All phases are mapped to values between 0 and 2π and represented by the black (zero phase) to gray (2π phase) scale in the 2D phase maps. The other parameters are the same as in Fig. 5.

the LGBs with several values of the radial and azimuthal modes. For $p = 0$, the associated Laguerre polynomial is constant and independent of ρ, because $L_0^1(2\rho^2/W^2(z)) = 1$. Therefore, the shape of the LGB for $l = 1$ appears as a single annular of intensity with a 2π phase singularity around the propagation beam axis. Our concentric annular rings for $l \neq 0$ of the radius proportional to $\sqrt{l}$ give beams which are called doughnut beams. They are bright rings around a central dark core, as shown in the second row in Fig. 7. The LGMs with $p = 0$ and $l \neq 0$ have a central minimum with the appropriate $\exp(-\mathrm{i}l\varphi)$ phase factor and a radius of maximum intensity scaled linearly with $\sqrt{l}$. This scaling proportional to $\sqrt{l}$ also applies to the divergence of OAM-carrying beams upon propagation, indicating that the LG_{pl} modes are endowed with the required feature of optical vortices. If we take $l = 0$ and $p \neq 0$, the number of nodes in the ring in the beam's intensity is $(p + 1)$, because the radial intensity pattern of LG beam exhibits $(p + 1)$ concentric bright high intensity rings around the beam propagation axis, which are shown in the first row in Fig. 7. It is visible in Fig. 8 (first row) that the phase distribution of the LGB displays concentric radial discontinuities with no smooth transitions at the beam waist plane $z = 0$. This contrast with the case when the phase depends on the azimuthal coordinate. Since the phase change in one round-trip around the beam axis is $\varphi = 2\pi$, when circulating around it, the total phase changes by $2\pi l$ during a full rotation around the propagation beam axis and is due to the azimuthal transverse phase term $\exp(-\mathrm{i}l\varphi)$, which is a result of the helical wavefronts. Consequently, for $l \neq 0$, there is a phase singularity at the center of the beam, where the intensity must be null because of the undefined phase at the end of each phase dislocation. Moreover, a phase singularity occurs, which produces an annular ring shape. Because of this singularity, LGBs are also called optical vortices [50-53]. This is shown in the second row in Figs. 7 and 8.

4. Laser beam profile analysis system

The block diagram of the experimental analysis system for the laser beam profile, which was developed to measure 2D and 3D intensity distributions using multiple scanning KEM and which is based on tomographic reconstruction, is shown in Fig. 9. The experimental set-up consists of:

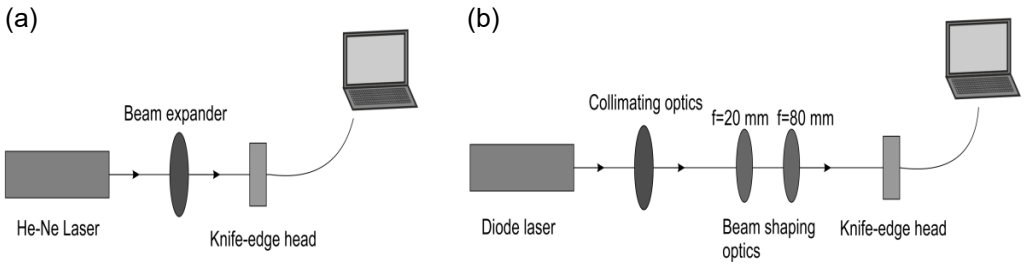

Fig. 9. Schematic illustration of the experimental set-up (a) He-Ne laser, (b) diode laser.

4.1. The laser's source

Two laser sources were used in this work. The He-Ne laser that emits 2.5 mW at a wavelength 632.8 nm, which has a beam diameter of 0.5 mm at the exit and a beam divergence of 1.5 mrad from the laser head, and the diode laser that emits 30 mW at a wavelength around λ = 830 nm, which was used for the same analysis. Many more measurements can be performed with different optical elements to expand, collimate, shape and focus the emitted beams. By using the shaped optics, the elliptical beam can be transformed into a circular one. The shaping optics (consisting of a set of cylindrical lenses with f = 20 mm and f = 80 mm, respectively) are shown in Fig. 9(b).

4.2. Beam width measurement using the multiple knife-edge method

The BeamMaster includes the BM-7 silicon detector head, with an active area of 9 × 9 mm, a computer plugin card, control software, and a 10% and 0.5% transmission optical filter. During the experiment, the knife-edge aperture passes between the near waist plane of the laser beam and the stationary power sensor (there is a certain period

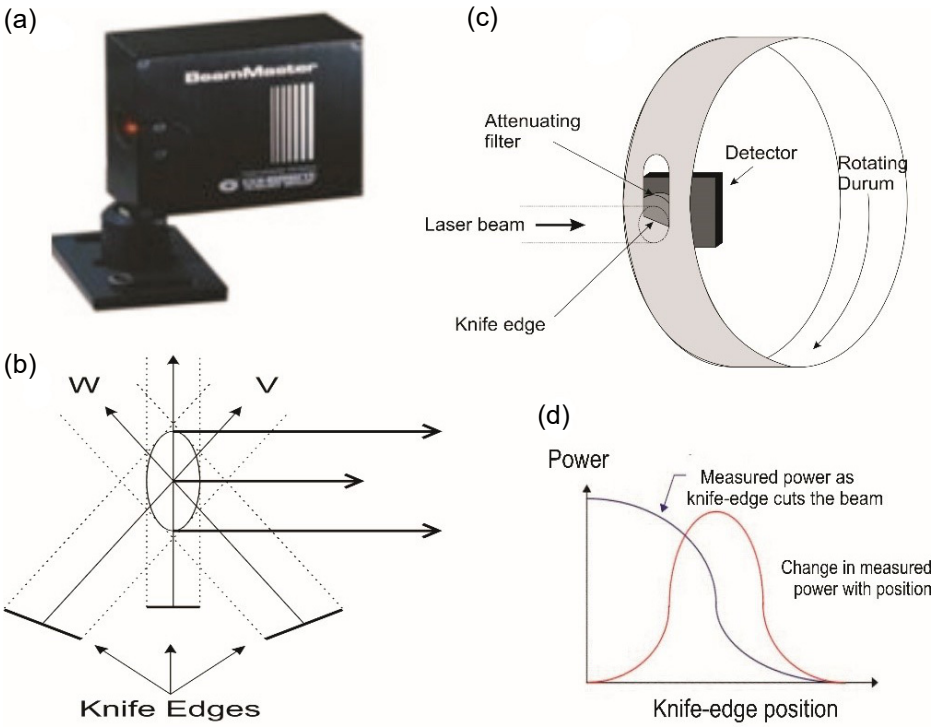

Fig. 10. (a) Seven axis knife-edge scanning instruments, (b) two primary knife-edges used for the main profile display, (c) the principle of scanning knife-edge beam profiling systems – a rotating drum is used to translate multiple apertures through the measurement plane, (d) the typical curve obtained during the measurement by the KEM.

of time where the center beam is allowed to reach the detector). Each of the seven individual scanning knife-edges is oriented at a different angle on the drum to scan the beam through seven different axes in a single rotation. This gives multiple axis cuts of the beam and the total transmitted power beam is measured to generate the 2D and 3D intensity profile of the GB from different directions of propagation. These beam profiles, called W and V, are perpendicular to each other and located at 45 degrees from the base of the detector head, as shown in Fig. 10(b). The profiles are used to provide the beam width, shape, position, power, and Gaussian fit analysis. Figure 10(a) shows a photograph of the seven-axis scanning knife-edge instrument. The mechanical layout of the BeamMaster PC detector head is shown in Fig. 10(c). The rotating drum contains multiple knife-edge apertures. As the apertures are scanned across the beam, the knife-edge blocks off an increasingly enlarged portion of the laser beam power. The detector head measures this change in total power versus the knife-edge position, creating the power or position plot, as shown in Fig. 10(d).

4.3. Relative total power

To scan the beam, the rotating drum in the detector head containing BM-seven knife -edge apertures is used. It moves across the beam path along different axes as the drum rotates. As a consequence, data from all seven scans are gathered as a result of more accurate measurements of the true beam shape, beam profile, beam size, position, and beam intensity profiles of the CW lasers. The wavelength λ range is from 400 to 1100 nm and the measurable beam size range $1/e^2$ is 30 μm up to 9 mm. The BM-7 silicon head containing the NG neutral density filter is inserted between the spinning drum and the head detector, where it introduces no distortion into the beam measurement, as shown in Fig. 10(c).

5. Results

Measurement of the intensity profile of the real laser beams is based on a multiple scanning KEM and tomagraphic image reconstruction. A spinning drum makes the knife -edges cut across the GB in an orthogonal plane to the direction of propagation. The real laser beam profile is perpendicular to the knife-edge. Each point of the profile is the sum of intensities along the axes of the knife-edge position in the x and y directions. An example of the measurement is shown in Fig. 11. The experimental results are similar to the theoretical ones. For the He-Ne laser, the shape correlations for the V and W directions are 93.3% and 96.4%, respectively. These are much better results when compared to the non-Gaussian shaped beam profile correlations for a diode laser of 88.4%, and 89%, respectively. The results were obtained at a low spatial resolution of 32×32, regardless of the beam size. For a diode laser where the beam distribution is significantly non-Gauusian, the standard seven knife-edge system can reconstruct a plot that closely matches the real beam. When examining the near-Gaussian beams,

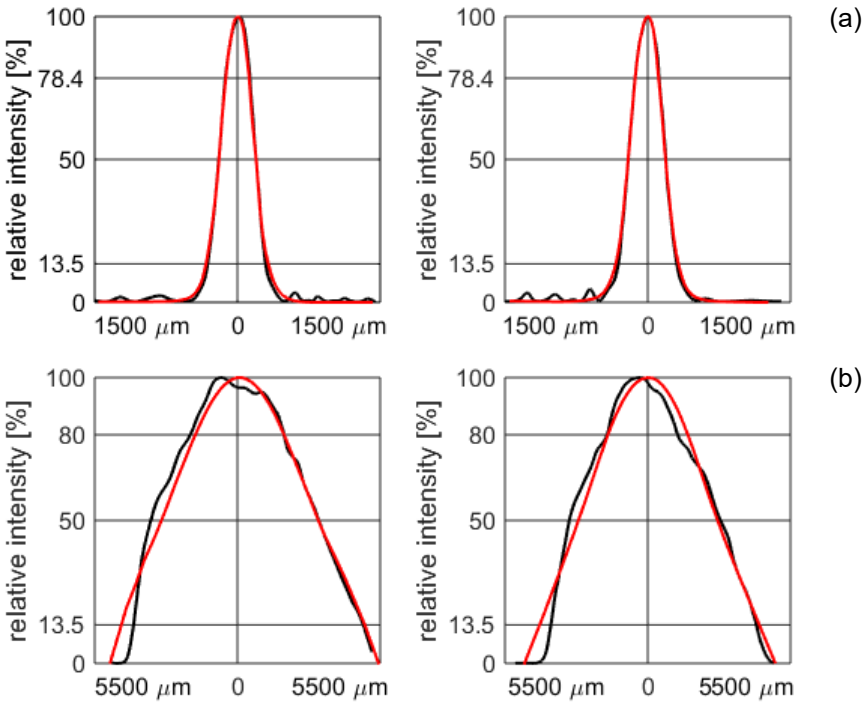

Fig. 11. Experimental (black) and theoretical (red) results of 2D relative intensity distributions of the FGM for (a) He-Ne laser beam profiles V (left) and W (right), (b) diode laser beam profiles V (left) and W (right) obtained using seven scanning KEM. The solid lines show the positions of $1/e^2$ intensity decreased to 13.5%, 50%, and 80%, respectively, of the peak intensity in the V and W direction.

the three knife-edge systems can give an accurate intensity distribution. Moreover, when measuring the beams that are far from a Gaussian shape, a high spatial resolution can be especially effective.

The results from the analysis of our experimental data for both the He-Ne laser and the diode laser are presented in Fig. 12. As can be clearly seen in Fig. 12(c, d), the transverse intensity in the cross-section plane of a He-Ne laser beam is circularly symmetric along the propagation axis, whereas it is elliptical in a diode laser, as shown in Fig. 12(a, b). This is due to the fact that the divergence in the x direction is different from that in the y direction. It can also be seen that there is a great difference in the distribution of intensity along the x axis and y axis, and therefore the intensity from a laser diode is not a Gaussian mode distribution. This ellipse is a "footprint" of the beam in the plane of the rotating knife-edges. It will change in shape and orientation as the beam expands and contracts in different directions. The 2D and 3D beam profiles are represented in color maps, in which red represents the greatest intensity and blue the minimum intensity. This result shows the capability of our system to analyze laser sources.

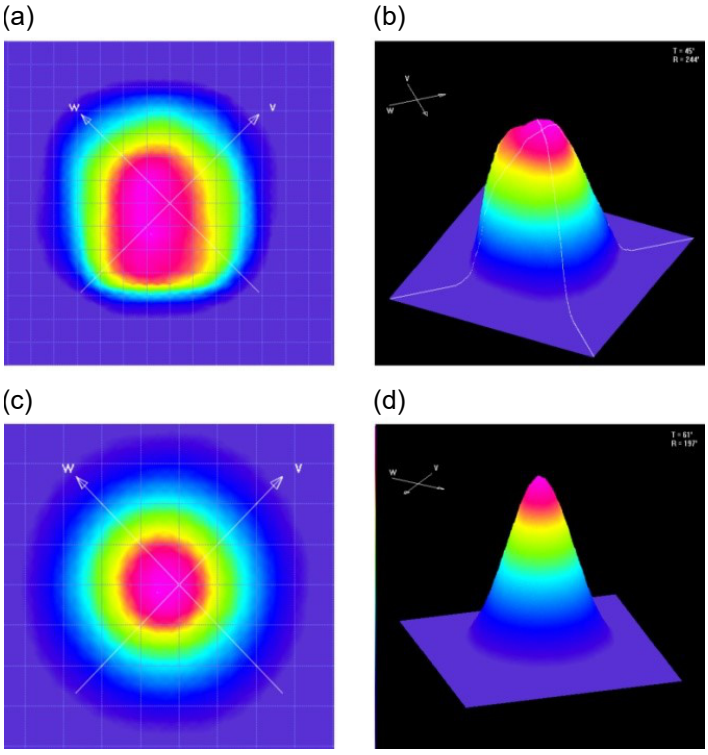

Fig. 12. Measured results of 2D and 3D intensity distributions of a FGM: (a,b) diode laser beam, (c,d) He-Ne laser using seven scanning KEMs.

The 2D and 3D normalized intensities of the He-Ne laser are shown in Fig. 13(a,b) for different distances of the observation plane. As can be seen in Fig. 13(a), the intensity distribution in the observation plane is rotationally symmetric. In Fig. 13(b), the intensity distribution near the observation plane no longer has rotational symmetry. The contour lines of equal intensity more or less resemble the shape of an ellipse. It can be noted from Fig. 13(a) that the shape of the beam intensity distribution is much better than the GB profile shown for comparison in Fig. 13(b). The shape of the GB depends on the position of the knife-edge apertures inserted between the initial and the observation planes. In addition, to insure the optimum measurement accuracy, the laser beam position should be centered in the detector area with no beam area overlapping the edge of the input aperture on the detector head. The incidence angle of the beam should also be normal to the face of the detector head. Finally, the beam spot size should not exceed the recommended minimum or maximum beam diameter for the detector head.

Finally, Fig. 14 shows the 3D normalized intensities of the diode laser profile of the GB for different directions of propagation with the use of the moving multiple KEM. The experimental results show that the diode laser emits an elliptical beam shape.

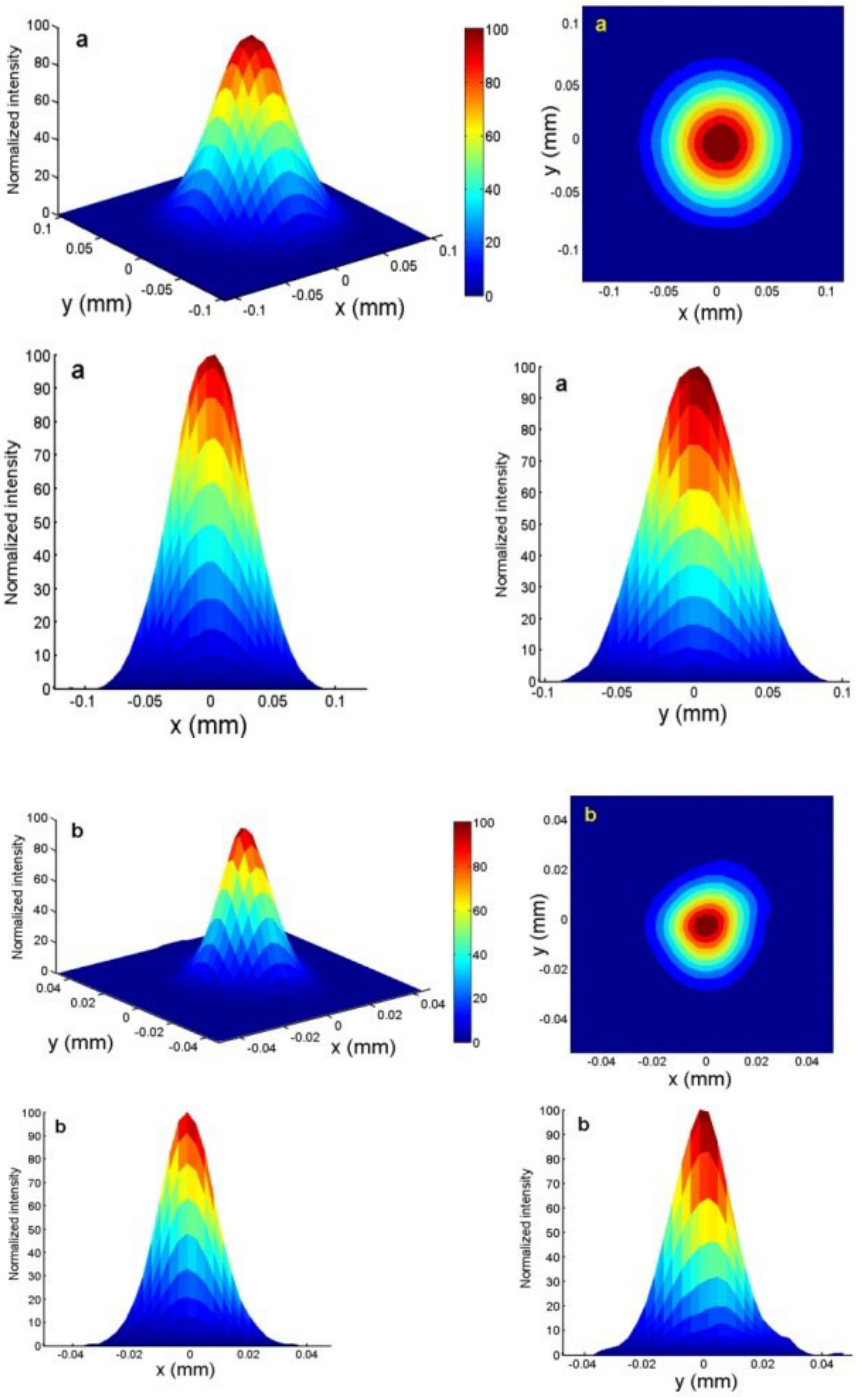

Fig. 13. The experimental results of the normalized intensity profile for the Gaussian He-Ne laser beam using seven scanning KEMs obtained at different observation planes.

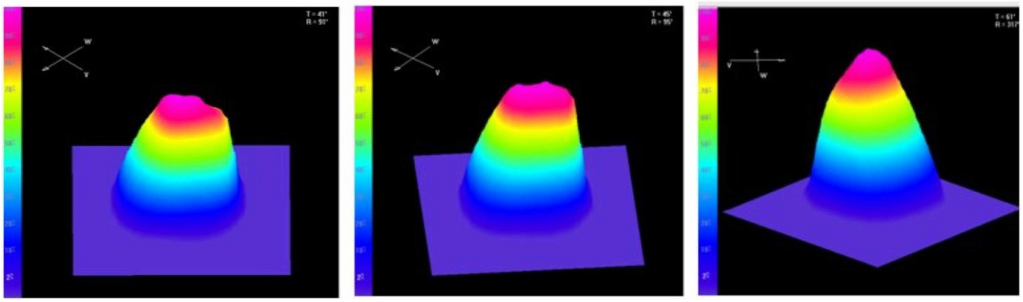

Fig. 14. The experimental results of the 3D normalized intensity profile for the Gaussian diode laser beam using seven scanning KEMs obtained at different observation planes.

6. Conclusions

The numerical model method, based on 2D FFT with ASM, for evaluating FGM, HGMs, and LGMs in free space propagation between two parallel planes has been introduced. This technique has proved to be accurate and useful to deepen the understanding of the propagation characteristics of GBs, HGBs, and LGBs. AS FFT algorithm can be considered as an alternative to the theoretical study, which is based on the Fresnel principle. The method was used to calculate the complex amplitude with its real and imaginary parts, the intensity, and the phase distributions for different order modes at different observation planes by using a computational program written in Borland C++Builder. Earlier results of the AS FFT algorithm verified its quality [34]. It significantly improves the numerical calculation efficiency and yields reliable results. Furthermore, the AS FFT algorithm can be applied in the full distance range without restriction on the far field. The analysis of the laser beam profiles of the FGM for the He-Ne laser and diode laser was experimentally carried out by using the tomographic method based on the multiple scanning KEM to obtain a series of intensity measurements along the propagation of the laser beam. The analysis of the laser beam shape, beam profile, beam size, position, and beam intensity using multiple KEM yields very detailed information on laser beams. The accuracy of all calculations will be affected by the beam peak intensity, centering size, and background noise. It was shown that the He-Ne laser emits a pure GB, whereas the diode laser emits an elliptical beam shape. It is important to have a tool for analyzing the structure of the beam shape for different types of lasers, because it is crucial to be sure that the demands for a particular application are fulfilled. This can be seen to have a big influence in laser printing, fiber optics coupling, material processing, optical data storage, or applications in medicine.

References

[1] Dickey F.M., *Laser Beam Shaping: Theory and Techniques*, CRC Press, New York, 2014.

[2] Masajada J., *Half-plane diffraction in the case of Gaussian beams containing an optical vortex*, Optics Communications **175**(4-6), 2000: 289-294. https://doi.org/10.1016/S0030-4018(00)00470-3

[3] GUTIÉRREZ-VEGA J.C., BANDERS M.A., *Helmholtz–Gauss waves*, Journal of the Optical Society of America A **22**(2), 2005: 289-298. https://doi.org/10.1364/JOSAA.22.000289
[4] WRIGHT D., GREVE P., FLEISCHER J., AUSTIN L., *Laser beam width, divergence and beam propagation factor: an international standardization approach*, Optical and Quantum Electronics **24**, 1992: S993 -S1000. https://doi.org/10.1007/BF01588600
[5] SIEGMAN A.E., *Lasers*, Oxford University Press, Mill Valley, CA, 1986.
[6] SIEGMAN A.E., *Hermite–Gaussian functions of complex argument as optical beam eigenfunctions*, Journal of the Optical Society of America **63**(9), 1973: 1093-1094. https://doi.org/10.1364/JOSA.63.001093
[7] CARBONE L., BOGAN C., FULDA P., FREISE A., WILLKE B., *Generation of high-purity higher-order Laguerre–Gauss beams at high laser power*, Physical Review Letters **110**, 2013: 251101-251106. https://doi.org/10.1103/PhysRevLett.110.251101
[8] SCHMIDT O.A., SCHULZE C., FLAMM D., BRÜNING R., KAISER T., SCHRÖTER S., DUPARRÉ M., *Real-time determination of laser beam quality by modal decomposition*, Optics Express **19**(7), 2011: 6741-6748. https://doi.org/10.1364/OE.19.006741
[9] ALSULTANNY Y.A., *Laser beam analysis using image processing*, Journal of Computer Science **2**(1), 2006: 109-113. https://doi.org/10.3844/jcssp.2006.109.113
[10] TSIGARIDAS G., FAKIS M., POLYZOS I., PERSEPHONIS P., GIANNETAS V., *Z-scan technique through beam radius measurements*, Applied Physics B **76**, 2003: 83-86. https://doi.org/10.1007/s00340-002-1067-5
[11] ARNAUD J.A., HUBBARD W.M., MANDEVILLE G.D., DE LA CLAVIERE B., FRANKE E.A., FRANKE J.M., *Technique for fast measurement of Gaussian laser beam parameters*, Applied Optics **10**(12), 1971: 2775-2776. https://doi.org/10.1364/AO.10.002775
[12] SUZAKI Y., TACHIBANA A., *Measurement of the μm sized radius of Gaussian laser beam using the scanning knife edge*, Applied Optics **14**(12), 1975: 2809-2810. https://doi.org/10.1364/AO.14.002809
[13] SIEGMAN A.E., SASNETT M.W., JOHNSTON T.F., *Choice of clip levels for beam width measurements using knife-edge techniques*, IEEE Journal of Quantum Electronics **27**(4), 1991: 1098-1104. https://doi.org/10.1109/3.83346
[14] CHAPPLE P.B., *Beam waist and M2 measurement using a finite slit*, Optical Engineering **33**(7), 1994: 2461-2466. https://doi.org/10.1117/12.169739
[15] KHOSROFIAN J.M., GARETZ B.A., *Measurement of a Gaussian laser beam diameter through the direct inversion of knife-edge data*, Applied Optics **22**(21), 1983: 3406-3410. https://doi.org/10.1364/AO.22.003406
[16] BACHMANN L., ZEZELL D.M., MALDONADO E.P., *Determination of beam width and quality for pulsed lasers using the knife-edge method*, Instrumentation Science & Technology **31**(1), 2003: 47-52. https://doi.org/10.1081/CI-120018406
[17] KIANG Y.C., LANG R.W., *Measuring focused Gaussian beam spot sizes: A practical method*, Applied Optics **22**(), 1983: 1296-1297. https://doi.org/10.1364/AO.22.001296
[18] HUBER C., ORLOV S., BANZER P., LEUCHS G., *Corrections to the knife-edge based reconstruction scheme of tightly focused light beams*, Optics Express **21**(21), 2013: 25069-25076. https://doi.org/10.1364/OE.21.025069
[19] MENDOZA-YERO O., ARRONTE M., *Determination of Hermite Gaussian modes using of the moving knife-edge*, Journal of Physics: Conference Series **59**, 2007: 497-500. https://doi.org/10.1088/1742-6596/59/1/107
[20] SINGH B.K., BAHL M., MEHTA D.S., SENTHILKUMARAN P., *Study of internal energy flows in dipole vortex beams by knife-edge test*, Optics Communications **293**, 2013: 15-21. https://doi.org/10.1016/j.optcom.2012.11.085
[21] SINGH B.K., MEHTA D.S., SENTHILKUMARAN P., *Visualization of internal energy flows in optical fields carrying a pair of fractional vortices*, Journal of Modern Optics **60**(13), 2013: 1027-1036. https://doi.org/10.1080/09500340.2013.828790
[22] ROSE A., NIE Y.-X., GUPTA R., *Laser beam profile measurement by photothermal deflection technique*, Applied Optics **25**(11), 1986: 1738-1741. https://doi.org/10.1364/AO.25.001738

[23] Baba T., Arai T., Ono A., *Laser beam profile measurement by a thermographic technique*, Review of Scientific Instruments **57**(11), 1986: 2739-2742. https://doi.org/10.1063/1.1139035

[24] de Araujo M.A.C., Silva R., de Lima E., Pereira D.P., de Oliveira P.C., *Measurement of Gaussian laser beam radius using the knife edge technique: improvement of data analysis*, Applied Optics **48**(2), 2009: 393-396. https://doi.org/10.1364/AO.48.000393

[25] González-Cardel M., Arguijo P., Díaz-Uribe R., *Gaussian beam radius measurement with a knife -edge: A polynomial approximation to the inverse error function*, Applied Optics **52**(16), 2013: 3849 -3855. https://doi.org/10.1364/AO.52.003849

[26] Quabis S., Dorn R., Eberler M., Glöckl O., Leuchs G., *The focus of light – theoretical calculation and experimental tomographic reconstruction*, Applied Physics B **72**, 2001: 109-113. https://doi.org/ 10.1007/s003400000451

[27] Marchenko P., Orlov S., Huber C., Banzer P., Quabis S., Peschel U., Leuchs G., *Interaction of highly focused vector beams with a metal knife-edge*, Optics Express **19**(8), 2011: 7244-7261. https://doi.org/10.1364/OE.19.007244

[28] Rico-García J.M., Sanchez-Brea L.M., Alda J., *Application of tomographic techniques to the spatial-response mapping of antenna-coupled detectors in the visible*, Applied Optics **47**(6), 2008: 768 -775. https://doi.org/10.1364/AO.47.000768

[29] Silva-López M., Rico-García J.M., Alda J., *Measurement limitations in knife-edge tomographic phase retrieval of focused IR laser beams*, Optics Express **20**(21), 2012: 23875-23886. https:// doi.org/10.1364/OE.20.023875

[30] Díaz-Uribe R., Rosete-Aguilar M., Ortega-Martínez R., *Position sensing of a Gaussian beam with a power meter and a knife edge*, Revista Mexicana de Física **39**(3), 1992: 484-492.

[31] Malacara D., *Optical Shop Testing*, 2nd Ed., Wiley-Inter-Science Publication, 1992.

[32] Talatinian A., *Numerical simulation of the physical properties of Gaussian mode using the angular spectrum technique*, Optik **127**(17), 2016: 6970-6977. https://doi.org/10.1016/j.ijleo.2016.05.009

[33] Talatinian A., *The analysis of the laser beam shape of the fundamental Gaussian mode by testing the numerical angular spectrum technique*, Optics & Laser Technology **118**, 2019: 75-83. https:// doi.org/10.1016/j.optlastec.2019.05.001

[34] Talatinian A., Pluta M., *Propagation of a fundamental laser mode and its numerical simulation by the angular spectrum technique*, Optik **127**(8), 2016: 3882-387. https://doi.org/10.1016/ j.ijleo.2016.01.111

[35] Talatinian A., *Far and near fields of Hermite–Gaussian beams passing through an annular aperture and its numerical simulation by the angular spectrum method*, Optica Applicata **53**(3), 2023: 467-481. https://doi.org/10.37190/oa230310

[36] Arlt J., *Handedness and azimuthal energy flow of optical vortex beams*, Journal of Modern Optics **50**(10), 2003: 1573-1580. https://doi.org/10.1080/09500340308235231

[37] Senthilkumaran P., *Optical phase singularities in the detection of laser beam collimation*, Applied Optics **42**(31), 2003: 6314-6320. https://doi.org/10.1364/AO.42.006314

[38] Lochab P., Senthilkumaran P., Khare K., *Near-core structure of a propagating optical vortex*, Journal of the Optical Society of America A **33**(12), 2016: 2485-2490. https://doi.org/10.1364/ JOSAA.33.002485

[39] Popiołek-Masajada A., Masajada J., Kurzynowski P., *Propagation of the vortex beam through the simple sample in the optical vortex microscope*, Proceedings of the SPIE, Vol. 10142, 20th Slovak -Czech-Polish Optical Conference on Wave and Quantum Aspects of Contemporary Optics, 2016: 1014206. https://doi.org/10.1117/12.2262432

[40] Szatkowski M., Burnecka E., Dyła H., Masajada J., *Optical vortex tracking algorithm based on the Laguerre–Gaussian transform*, Optics Express **30**(10), 2022: 17451-17464. https://doi.org/ 10.1364/OE.455502

[41] Goodman J.W., *Introduction to Fourier Optics*, 3nd Ed., Roberts & Company, 2005.

[42] Saghafi S., Sheppard C.J.R., *The beam propagation factor for higher order Gaussian beams*, Optics Communications **153**(4-6), 1998: 207-210. https://doi.org/10.1016/S0030-4018(98)00256-9

[43] BYRON F.W., FULLER R.W., *Mathematics of Classical and Quantum Physics*, Vol. 2, Addison-Wesley, Massachusetts 1972.

[44] ALLEN L., BEIJERSBERGEN M.W., SPREEUW R.J.C., WOERDMAN J.P., *Orbital angular momentum of light and the transformation of Laguerre–Gaussian laser modes*, Physical Review A **45**, 1992: 8185 -8189. https://doi.org/10.1103/PhysRevA.45.8185

[45] ALLEN L, BARNETT S.M., PADGETT M.J., *Optical Angular Momentum*, Institute of Physics Publishing, Bristol, 2003.

[46] ALLEN L., PADGETT M.J., BABIKER M., *The orbital angular momentum of light*, Progress in Optics **39**, 1999: 291-372. https://doi.org/10.1016/S0079-6638(08)70391-3

[47] PADGETT M.J., ALLEN L., *The Poynting vector in Laguerre–Gaussian laser modes*, Optics Communications **121**(1-3), 1995: 36-40. https://doi.org/10.1016/0030-4018(95)00455-H

[48] FENG S., WINFUL H.G., *Physical origin of the Gouy phase shift*, Optics Letters **26**(8), 2001: 485-487. https://doi.org/10.1364/OL.26.000485

[49] PETERSEN T.C., PAGANIN D.M., WEYLAND M., SIMULA T.P., EASTWOOD S.A., MORGAN M.J., *Unifying interpretations of the Gouy phase anomaly for electron waves*, Physical Review **89**, 2014: 063801. https://doi.org/10.1103/PhysRevA.89.063801

[50] PADGETT M.J., MIATTO F.M., LAVERY M.P.J., ZEILINGER A., BOYD R.W., *Divergence of an orbital -angular-momentum carrying beam upon propagation*, New Journal of Physics **17**, 2015: 023011. https://doi.org/10.1088/1367-2630/17/2/023011

[51] ZOLNACZ K., SZATKOWSKI M., MASAJADA J., URBANCZYK W., *Broadband chromatic dispersion measurements in higher-order modes selectively excited in optical fibers using a spatial light modulator*, Optics Express **29**(9), 2021: 13256-13268. https://doi.org/10.1364/OE.422736

[52] SZATKOWSKI M., POPIOŁEK-MASAJADA A., MASAJADA J., *Beam quality measurement through off-axis optical vortex*, Proceedings of the SPIE, Vol. 11107, Laser Beam Shaping XIX, 2019: 1110703. https://doi.org/10.1117/12.2529779

[53] SZATKOWSKI M., POPIOŁEK-MASAJADA A., MASAJADA J., *Optical vortex trajectory as a merit function for spatial light modulator correction*, Optics and Lasers in Engineering **118**, 2019: 1-6. https://doi.org/10.1016/j.optlaseng.2019.01.014

Received May 12, 2023